Journal of Energy Challenges and Mechanics
http://www.nscj.co.uk/JECM/
ISSN 2056-9386
Volume 2 (2015) issue 4, article 2

The role of deformation history of buckle folds on sustainable pore pressure magnitudes

褶皱构造过程对于可持续孔隙压力影响的研究

Andreas Eckert[1*], Xiaolong Liu[1]

[1] *Department of Geosciences and Geological and Petroleum Engineering, Missouri University of Science and Technology, Rolla, MO 65409, USA*

eckertan@mst.edu

Accepted for publication on 22nd October 2015

Abstract - **Subsurface engineering applications such as waste water disposal or CO_2 sequestration require the selection of suitable injection sites which depends critically on the assessment of geomechanical risks such as fracture initiation or fracture reactivation. As an analogue to hydrocarbon production sites, buckle fold structures are a preferred structural trap for fluid storage and become of interest for waste water disposal or CO_2 sequestration. In this contribution, 3-dimensional finite element analysis is used to quantify the influence of different permeability distributions in a multi-layer visco-elastic buckle fold system on the resulting state of stress throughout the deformation history of the fold. Based on the advanced, tensor based concept of pore pressure – stress coupling, pre-injection analytical estimates of the maximum sustainable pore pressure change, ΔPc, for fluid injection scenarios can be calculated if the state of stress of a geologic structure can be quantified using numerical models. The results of this study show that the minimum ΔPc is varying throughout the deformation history of multilayer buckle folds and different locations within the structure show great variability in ΔPc. Furthermore, the permeability distribution of the various layers in the multilayer fold system has great influence on minimum ΔPc. It is concluded that geomechanical risk assessment for active fold belts needs to consider the complete deformation history of geologic structures such as buckle folds.**

Keywords – **multilayer buckle folds, sustainable pore pressure, deformation history, erosional unloading.**

*关键词 - 多岩层弯曲褶皱，可持续孔隙压力，构造变形史，*剥蚀反弹。

I. INTRODUCTION

The reactivation of critically stressed fractures due to subsurface fluid injection represents a geomechanical risk for applications such as waste water disposal or geologic CO_2 sequestration. As shown by [1], the lower limit of sustainable subsurface pore pressures is determined by the threshold of reactivation of optimally oriented, cohesionless shear fractures. If reactivated these fractures represent fluid flow pathways [2] which may connect the fluid reservoir to the surface or to fresh water aquifers and fluid injection related seismicity is observed [3-7]. Geomechanical risk assessment of fracture reactivation [e.g. 6, 8-13] requires a thorough understanding of the in situ state of stress and the pore pressure distribution and evolution, which often involves extensive numerical modeling studies coupling geomechanics to fluid flow through porous media [10,12,14-17]. As a result from these studies it has been concluded that the fluid flow boundary conditions [10,18,19] and the in situ stress regime [10,11,20] are the key parameters determining the likelihood of fracture reactivation.

As an alternative the tensor based concept of pore pressure – stress coupling [21,22] can be used to calculate analytical pre-injection estimates of the maximum sustainable pore pressure [20]. The pore pressure – stress coupling (PPSC) theory states that the principal stress magnitudes change with a change in pore pressure. [22] showed that PPSC is different for different stress regimes and that (for a homogenous full space) the risk of fault reactivation is highest along the maximum principal stress direction. The homogeneous full space modeling results by [22] imply on the assumption of the prevailing stress regimes being Andersonian (i.e. compressional, strike-slip and extensional). [20] showed that the PPSC principle can be applied to any state of stress and thus be applied to complex geologic structures where stresses are not Andersonian. As long as the principal stress magnitudes and orientations can be determined (e.g. using numerical modeling approaches such as finite element analysis) the maximum sustainable change in pore pressure magnitude, ΔP_c, prior to injection can be calculated for the complete structure. PPSC accounts for the poro-elastic effects

and over- or underestimations of ΔP_c can be minimized [11,22].

For safe long term sub-surface storage of fluids natural geologic trap systems such as fold structures become of primary interest. In their study, [20] have applied the PPSC principle to anticline structures subject to different stress regimes and different levels of inter-layer coupling using 3D finite element analysis. However, the anticline structures considered are based on static representations of stress and pore pressure, i.e. the specific strain path of how the geologic system evolved is not considered. [23-25] have shown that the stress and pore pressure distribution in single- and multi-layer buckle folds vary significantly throughout the deformation history and with respect to the permeability distribution of the modeled layers. In addition to the structural development, post-deformation processes such as erosional unloading during exhumation have significant influence on the resulting stress distribution [23,26].

In this contribution, 3D finite element analysis is used to simulate the stress and pore pressure distribution of visco-elastic multi-layer buckle fold systems. The modeled fold systems are characterized by permeability distributions resembling favorable cap rock (i.e. low permeability) and injection layer (i.e. high permeability) sequences. Based on the resulting state of stress and pore pressure evolution of the fold system during the deformational history (including erosional unloading strain paths) the maximum sustainable pore pressure change, ΔP_c, is quantified and the risk of fracture reactivation assessed.

II. Pore Pressure – Stress Coupling

In contrast to the to the previous concept of PPSC described by [27,28], not only the minimum horizontal stress, but all principal stress components are affected by changes in pore pressure [21,22]. As a result the ratio of $\Delta\sigma_{ij} / \Delta P$ is a complex function of space ($\vec{x}$) and time (t) and has tensor character. The simplification of the long term limits (i.e. $t \to \infty$; which becomes relevant for subsurface fluid injection scenarios requiring an estimate of the sustainable pore pressure change over long time periods) results in the following coupling ratios for the radial (σ_{rad}) and tangential (σ_{tan}) stress components [29] in a principal coordinate system (Figure 1; after [21]) are given:

$$\lim_{t\to\infty} \frac{\Delta\sigma_{rad}(\vec{x},t)}{\Delta P(\vec{x},t)} = \alpha\frac{1-2\nu}{1-\nu} \tag{1}$$

$$\lim_{t\to\infty} \frac{\Delta\sigma_{\tan}(\vec{x},t)}{\Delta P(\vec{x},t)} = \frac{1}{2}\alpha\frac{1-2\nu}{1-\nu} \tag{2}$$

where α represents the Biot coefficient and ν the Poisson's ratio. The full tensor solution of the PPSC equations are given in [20,21]. [21] showed that based on the new effective stress tensor after injection the maximum sustainable pore pressure, P_c, for fault reactivation can be derived for each principal stress direction. They also show that the lowest P_c is obtained for the σ_1 direction and is given by:

$$P_c = \frac{b\sigma_3 - \sigma_1 - \left(\alpha\frac{1-2\nu}{1-\nu}\right)(\frac{b}{2}-1)P}{\alpha\frac{1-2\nu}{1-\nu}(1-\frac{b}{2}) - (1-b)} \tag{3}$$

where b is given by $b = \frac{1+\sin\phi}{1-\sin\phi}$, with ϕ being the angle of internal friction, and P is the initial pore pressure. The maximum sustainable change in pore pressure magnitude, ΔP_c,is then calculated by:

$$\Delta P_c = P_c - P \tag{4}$$

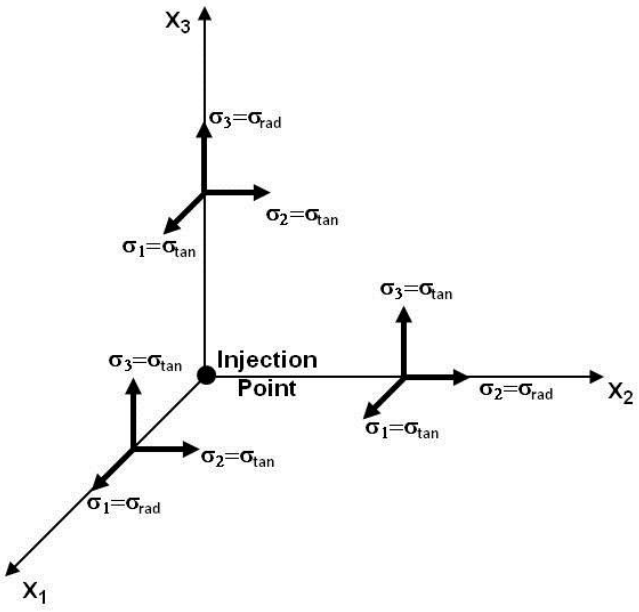

Figure 1: Principal axis coordinate system with different stress components, σ_1, σ_2, and σ_3, which are represented as radial and tangential stresses along different axes with respect to the injection location (after [21]).

III. Numerical Modeling Approach

2.1. Visco-elastic Buckle folding

In this study a classic Maxwell model (allowing instantaneous elastic behavior for high strain rates and time dependent viscous behavior for low strain rates) is adopted to simulate visco-elastic, multi-layer layer, cylindrical buckle fold systems [23-25]. Pore pressure is introduced by utilizing effective stress analysis assuming an incompressible fluid and rock matrix, i.e. utilizing a Biot coefficient of α=1 [30]. The governing equation system is presented in detail by [23] and thus not repeated here. A 3D finite element analysis (FEA; via the commercial software package ABAQUS™) is employed to solve the equations of equilibrium, conservation of mass, constitutive equations, and the equations for pore fluid flow.

The numerical models are setup such that only one wavelength, i.e. the dominant wavelength λ_{dv} ($\frac{\lambda_{dv}}{h} = 2\pi\sqrt[3]{\frac{N\mu_f}{6\mu_m}}$, where *N* is the number of competent layers, *h* is the layer thickness; μ_f and μ_m represent the viscosities of the folded layer and the surrounding rock matrix, respectively) is amplified [23]. As presented in [23,24] the parameter R (the ratio between the viscous dominant wavelength, λ_{dv}, and the elastic dominant wavelength, λ_{de}) is utilized to determine whether the competent layer is folded viscously (R<1) or elastically (R>1) [31,32]. Based on the material properties used (i.e. $\mu_f = 10^{21}$ Pa s, G ≈12 GPa) R equals 0.134. This indicated predominantly viscous deformation and an appropriate viscous dominant wavelength of 630.96 m is chosen for the geometry of the initial perturbation.

2.1. Model Setup

The 3D model geometry features a multi-layer fold structure comprised of 5 layers, of 30m thickness each, embedded in a rock matrix of varying thickness (Figure 2; Table 1). The horizontal model dimensions are 150 m by 2839 m. The 5 fold layers are characterized by small periodic perturbations of the viscous dominant wavelength with 2.5m amplitude. The 5 fold layers and the matrix surrounding them feature a viscosity and stiffness contrast (Table 1), whereby Layers 1, 3, and 5 represent the more competent layers (i.e. having higher Young's modulus and higher viscosity). In addition to the competence contrast different permeabilities are assigned to the matrix and fold layers to represent a cap rock – injection layer sequence (Table 1). Considering the significant overburden load applied in this study, initial porosity decreases with depth and is assigned after [33]:

$$\varphi(z) = 16.39e^{-0.00039z} \quad (5)$$

where ϕ is the porosity (%), and *z* is the depth in meters below the top of the overburden. Furthermore, since permeability also changes with depth, the relationship given by [33] is modified and applied to represent high and low horizontal permeabilities in models with overburden less than 1500 meters as:

$$k_H(z) = 7.583\cdot10^{-17}e^{0.283\phi} \quad (6)$$

$$k_H(z) = 7.583\cdot10^{-23}e^{0.283\phi} \quad (7)$$

and in models with overburden more than 1500 meters as:

$$k_H(z) = 7.583\cdot10^{-16}e^{0.283\phi} \quad (8)$$

$$k_H(z) = 7.583\cdot10^{-22}e^{0.283\phi} \quad (9)$$

where ϕ is the porosity (in %), *z* is the depth in meters and *k* is the permeability in m^2. The anisotropic permeability ratio (i.e. k_H/k_v) equals to 5.

Since the permeability magnitude has significant influence on the resulting pore pressure distribution [23, 25], 2 model scenarios with either the competent layers being permeable or the incompetent layers being permeable are considered (Tables 1,2). The models are subjected to 2 or 3 different load steps respectively (Table 3). The first load step features the equilibration of the gravitational compaction (termed pre-stressing) of the model [23-25]; in the second load step the model is compressed with a strain rate of 10^{-14} s^{-1} [34] until 50% of bulk shortening is obtained; the third load step applies uni-axial erosional unloading (Figure 2b) with an exhumation rate of 1 mm/a [34]. The overburden thickness for the various models is varied considering the different load steps (Table 3). For models featuring the buckling process only (Models 1 & 2; Table 3) an overburden thickness of 1000 m is chosen. Models also subjected to erosional unloading (Models 3 & 4; Table 3) have an overburden 3000 m thick. For the erosional unloading models different deformation stages (i.e. different amounts of bulk shortening) are considered before the onset of exhumation.

The initial pore pressure distribution during the gravitational compaction is hydrostatic. The fluid flow boundary conditions represent a semi-closed system [18] such that fluid flow is constrained across the lateral model boundaries but pressure dissipation occurs vertically.

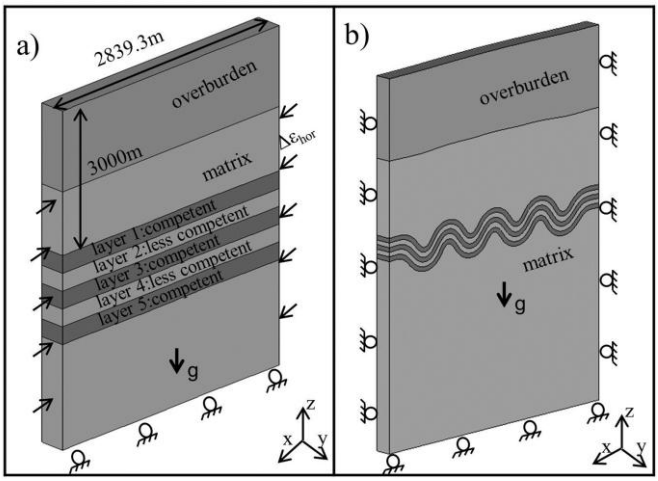

Figure 2: Model geometry and boundary conditions.

Table 1: Material properties for the various models. All model parts feature a Poisson's ratio of ν=0.25.

	E (GPa)		μ (10^{21} Pa·s)	
	Model 1&2	**Model 3&4**	**Model 1&2**	**Model 3&4**
Overburden	2.85(0.5km)	3.03(1.5km)	0.0133	0.0133
Layer 1	29.9	31.93	1	1
Layer 2	2.99	3.193	0.0133	0.0133
Layer 3	29.9	31.93	1	1
Layer 4	2.99	3.193	0.0133	0.0133
Layer 5	29.9	31.93	1	1
Underburden	3.03(1.5km)	3.23(3.5km)	0.133	0.133

Table 2: Horizontal permeabilties for the various models

	Model 1	Model 2	Model 3	Model 4
Overburden	3.44×10^{-15} (0.5km)	3.44×10^{-15} (0.5km)	1×10^{-14} (1.5km)	1×10^{-14} (1.5km)
Layer 1	1.75×10^{-21}	1.75×10^{-15}	3.20×10^{-21}	3.20×10^{-15}
Layer 2	1.75×10^{-15}	1.75×10^{-21}	3.20×10^{-15}	3.20×10^{-21}
Layer 3	1.75×10^{-21}	1.75×10^{-15}	3.20×10^{-21}	3.20×10^{-15}
Layer 4	1.75×10^{-15}	1.75×10^{-21}	3.20×10^{-15}	3.20×10^{-21}
Layer 5	1.75×10^{-21}	1.75×10^{-15}	3.20×10^{-21}	3.20×10^{-15}
Underburden	1×10^{-15} (1.5km)	1×10^{-15} (1.5km)	2.48×10^{-15} (3.5km)	2.48×10^{-15} (3.5km)

Table 3: Various types of loading and overburden thicknesses for the models considered.

Model	**Load steps**	**Overburden thickness**
1-2	Pre-stressing Buckling	1000 m
3-4	Pre-stressing Buckling Erosional unloading	3000 m

III. Model Results

In order to assess the critical sustainable pore pressure after Eq. (3) and (4) we assume a value of 30° for the angle of internal friction. The results for ΔP_c are plotted for deformation stages of 10, 20, and 30% of bulk shortening. Larger bulk shortening leads to fold structures with high fold limb dips which are more unlikely to be considered. For the following results analysis the contours of ΔP_c magnitudes at the various deformation stages are presented in combination with the according σ_1 directions. It should be noted that the results description and analysis is focused on the cap rock layers of the respective models considered.

3.1. Model 1

In Model 1 the competent layers (Layers 1, 3, 5) of the multi-layer fold system feature a low permeability and thus represent possible cap rock sequences. While the results for 10% shortening (Fig. 3a) show positive ΔP_c magnitudes of 7.5-9.5 MPa (Layer 4) and 9.5-13 MPa (Layer 2) for the injection layers, the stiffer cap rock layers (Layers 1, 3, 5) show widespread risk of fracture reactivation, i.e. ΔP_c magnitudes of 0 MPa (grey contours in Fig. 3a) throughout large parts of the cap rock layer. The stress orientations display that σ_1 is oriented layer parallel / sub-parallel in Layer 1 and 3. In Layer 5, σ_1 becomes vertical at the top of the fold hinge.

While widespread failure and low ΔP_c magnitudes are still observed at 20% of shortening for the lowest cap rock layer (Figure 3b), the immediate risk of fracture reactivation reduces significantly in the central cap rock layer (Layer 3). Although ΔP_c magnitudes are 0 in a small stretch at the top and the bottom of the hinge zone (Fig. 3b), the centre of this layer has ΔP_c magnitudes of 6.5-10 MPa. ΔP_c magnitudes in the limb are slightly larger (7-11MPa). The top cap rock layer features even higher ΔP_c magnitudes ranging from 8 MPa at the bottom of the hinge to 16.5 MPa towards the top of the hinge (Fig. 3b) and in the limb. ΔP_c magnitudes of 0 MPa are only observed in the synform part of the fold. The σ_1 orientations in the folded layers, which are characterized by higher amplitudes at 20%, show a more pronounced separation from layer parallel / sub-parallel at the bottom of the hinge to σ_1 becoming vertical at the top of the fold hinge, which represents common stress orientations in buckle folds [23,25].

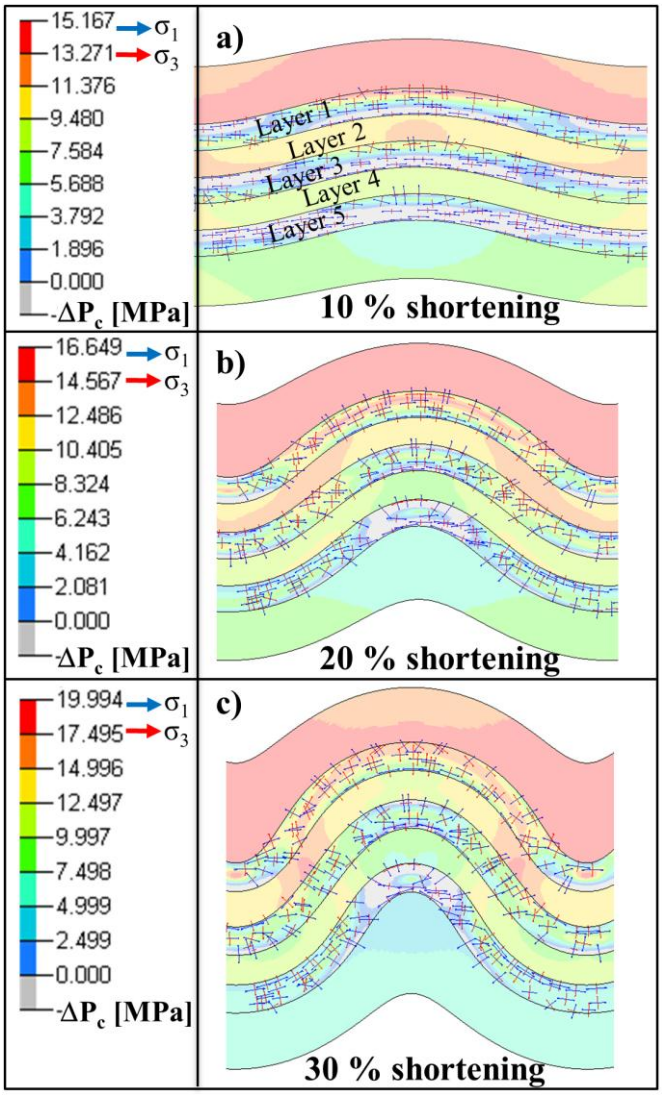

Figure 3: ΔP_c magnitudes and principal stress orientations for Model 1 for 10%, 20% and 30% of bulk shortening.

At 30% of shortening (Fig. 3c) the same pattern of ΔP_c magnitudes can be observed as for 20% of shortening, yet with slightly increased ΔP_c magnitudes. The lowest cap rock features immediate risk of fracture reactivation (ΔP_c ranging from 0-5MPa). For the central cap rock layer ΔP_c magnitudes range from 0MPa at the very top and bottom of the hinge zone to ~12.5MPa in the centre of the hinge zone and 10-12 MPa throughout the fold limb. The top cap rock layer features the

highest ΔP_c magnitudes ranging from 8-17.5 MPa. The stress orientations are similar to 20%.

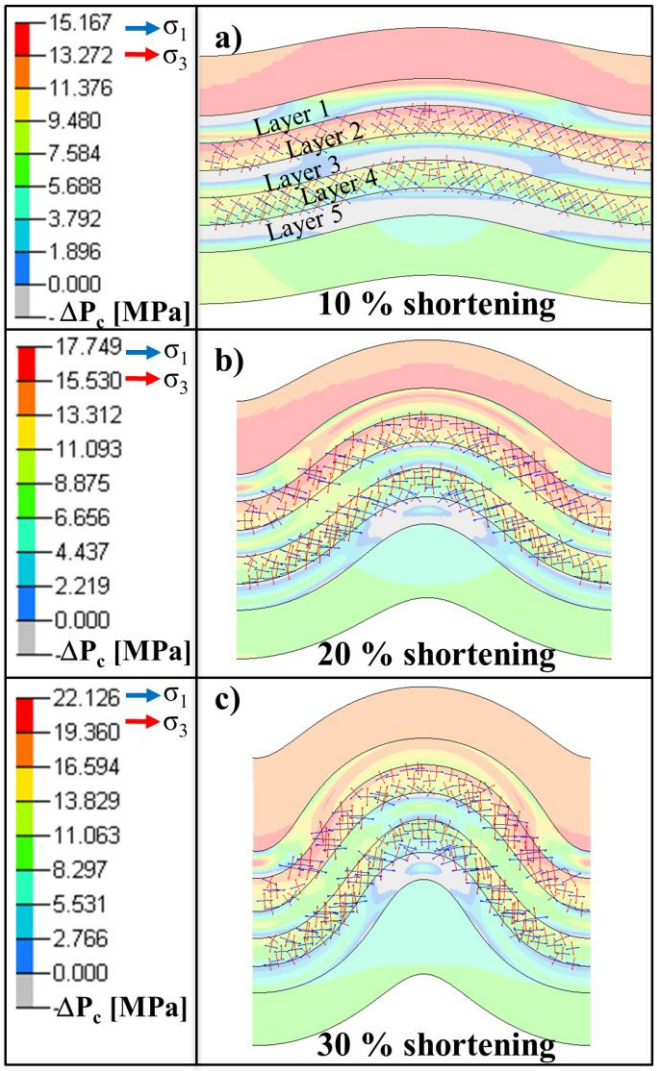

Figure 4: ΔP_c magnitudes for Model 2 for 10%, 20% and 30% of bulk shortening.

3.2. Model 2

In contrast to Model 1, in Model 2 the incompetent layers of the multi-layer fold system feature a low permeability, and hence only Layer 3 and 5 can be considered as injection layers.

The results for 10% shortening (Fig. 4a) show that both cap rock layers feature positive ΔP_c magnitudes while the injection layers show risk of fracture reactivation (i.e. ΔP_c =0). For Layer 2, ΔP_c magnitudes range from 9.5 MPa at the bottom of the layer to 15 MPa at the top of the layer. For Layer 4, ΔP_c magnitudes are lower, ranging from 5.5 MPa at the bottom of the layer to 9 MPa at the top of the layer. The σ_1 orientations do not resemble common patterns as observed for Model 1; σ_1 is orientated oblique (at an angle of ~ ± 45°) throughout both Layers 2 and 4.

For 20% (Fig. 4b) and 30% (Fig. 4c) of shortening the ΔP_c magnitudes generally increase throughout the cap rock layers. In Layer 2, ΔP_c increases to 11-17.5 MPa (at 20%) and 13-19 MPa (at 30%). For Layer 4, ΔP_c has magnitudes of 6-11MPa at 20% and 5-14 MPa at 30%. The σ_1 orientations at 20% and 30% maintain the oblique angle at the bottom of the hinge zone and at the bottom of the limb, but rotate towards σ_1 being horizontal at the top of the hinge. This is in contrast to the commonly expected stress orientations at the top of fold hinges [23,25].

3.3. Model 3

The stiffness and permeability distribution in Model 3 is equivalent to Model 1, although Model 3 features an initial overburden thickness of 3000 m and as a result of the increased compression ΔP_c magnitudes are much higher.

After 10% of shortening (Fig. 5a) the top cap rock layer (Layer 1) displays ΔP_c magnitudes of 30-45 MPa throughout the layer. The second cap rock layer (Layer 3) shows ΔP_c ranging from 17-30 MPa. The lowest cap rock layer (Layer 5) features the lowest ΔP_c magnitudes with imminent risk of fracture reactivation (i.e. $\Delta P_c = 0$) at the bottom of the hinge zone. In the fold limb and towards the top of the hinge zone ΔP_c magnitudes increase to 10-17 MPa.

For 20% of shortening (Fig. 5b) and 30% of shortening (Fig. 5c) a similar distribution of ΔP_c magnitudes is observed for the various layers, featuring increased numbers to the increasing overburden thickness. For Layer 1 ΔP_c ranges between 40-47 MPa (20%) and 47-56 MPa (30%); for Layer 3 ΔP_c ranges between 27-34 MPa (20%) and 32-39 MPa (30%); Layer 5 featuring the lowest ΔP_c magnitudes with ΔP_c reaching 0 MPa at the top of the hinge zone (both at 20% and 30%) and ranging from 6-20 MPa (20%) and 7-23 MPa (30%) throughout the fold.

The stress orientations throughout the shortening stages of the model are similar to Model 1.

In order to investigate the influence of erosional unloading and exhumation processes Fig. 6 shows ΔP_c magnitudes after erosional unloading is applied to the model after the various shortening stages.

For 10% of shortening followed by erosional unloading over 2.06 Ma (with a remaining overburden thickness of 1071 m) it is observed that the top cap rock layer (Layer 1) is prone to fracture reactivation throughout the layer (Fig. 6a). For Layer 3 fracture reactivation occurs at the bottom of the hinge zone and ΔP_c magnitudes range between 0 -12 MPa at the top of the hinge zone and 3-10 MPa in the fold limb. For the lowest cap rock layer (Layer 5) ΔP_c magnitudes range from 1 MPa at the bottom of the hinge to 21 MPa at the top of the hinge zone; ΔP_c magnitudes in the fold limb are ~15 MPa. The stress orientations do not significantly change compared to the shortening stage.

The same behavior for the ΔP_c magnitudes can be observed for 20% (Fig. 6b) and 30% (Fig. 6c) of shortening followed by erosional unloading over 2.37 Ma and 2.039 Ma, respectively (with a remaining overburden thickness of 1349 m and 2253 m,

respectively): i.e. overall lower ΔP_c magnitudes; widespread risk of fracture reactivation in Layer 1; localized fracture reactivation at the bottom of the hinge in Layer 3 and only minor risk of fracture reactivation in Layer 5.

Considering the principal stress orientations, significant differences occur after erosion following 20% of shortening: in Layer 1 σ_1 becomes fold parallel (i.e. the out-of plane component in Fig. 6) in the limb and at the top of the hinge zone; in the bottom of the hinge zone σ_1 is horizontal / layer parallel; in Layer 3 σ_1 is mostly horizontal / layer parallel in the hinge zone and parallel to the hinge line in the fold limb; in Layer 5 σ_1 is layer perpendicular in the limb, horizontal at the bottom of the hinge and vertical at the top of the hinge.

For 30% followed by erosion σ_1 orientation in Layer 1 is similar to 20%; in Layer 3 σ_1 is horizontal at the fold hinge and layer perpendicular in the fold limb; in Layer 5 σ_1 is horizontal at the fold hinge but does not show a consistent orientation in the fold limb.

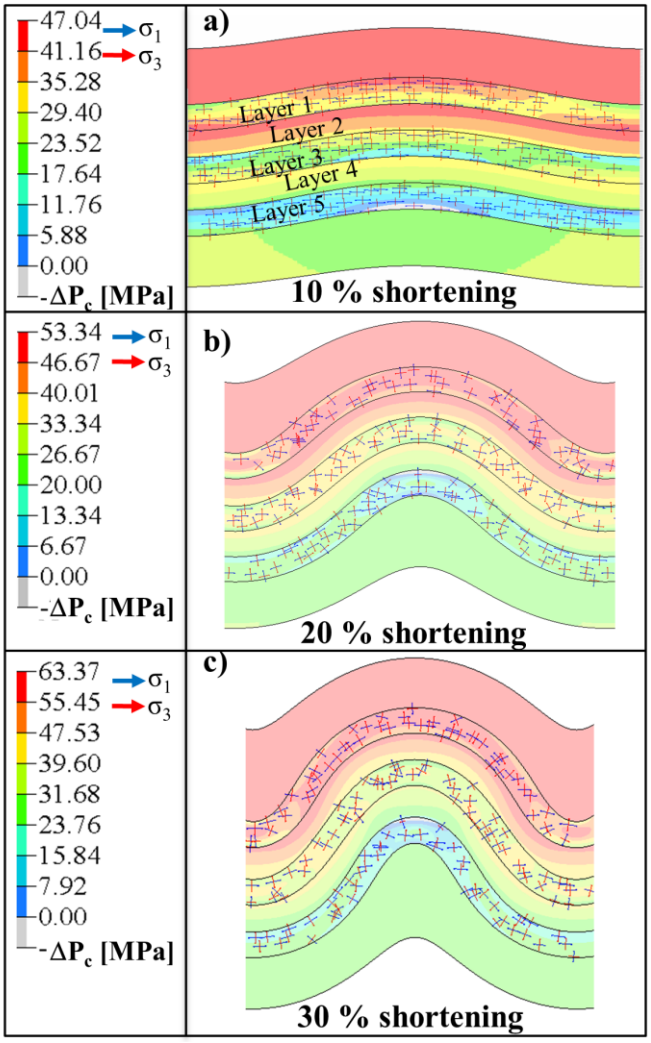

Figure 5: ΔP_c magnitudes for Model 3 for 10%, 20% and 30% of bulk shortening.

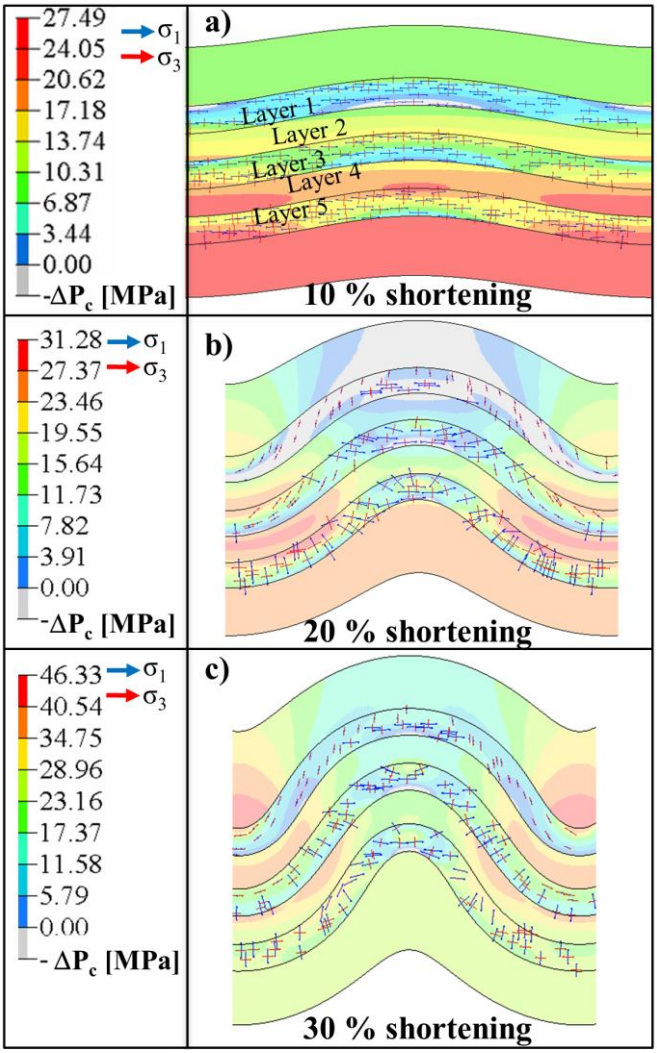

Figure 6: ΔP_c magnitudes for Model 3 after erosional unloading is applied.

The significant decrease in ΔP_c magnitudes due to erosional unloading can be explained by considering the evolution of the principal effective stresses at the top and bottom of the fold hinge of Layer 1. Figure 7a,b (showing this exemplarily for the 10% shortening model) shows that the minimum effective principal stress, σ'_3, decreases much more rapidly than the maximum effective principal stress, σ'_1, hence increasing the differential stress and reducing the ΔP_c magnitudes throughout the erosional unloading process.

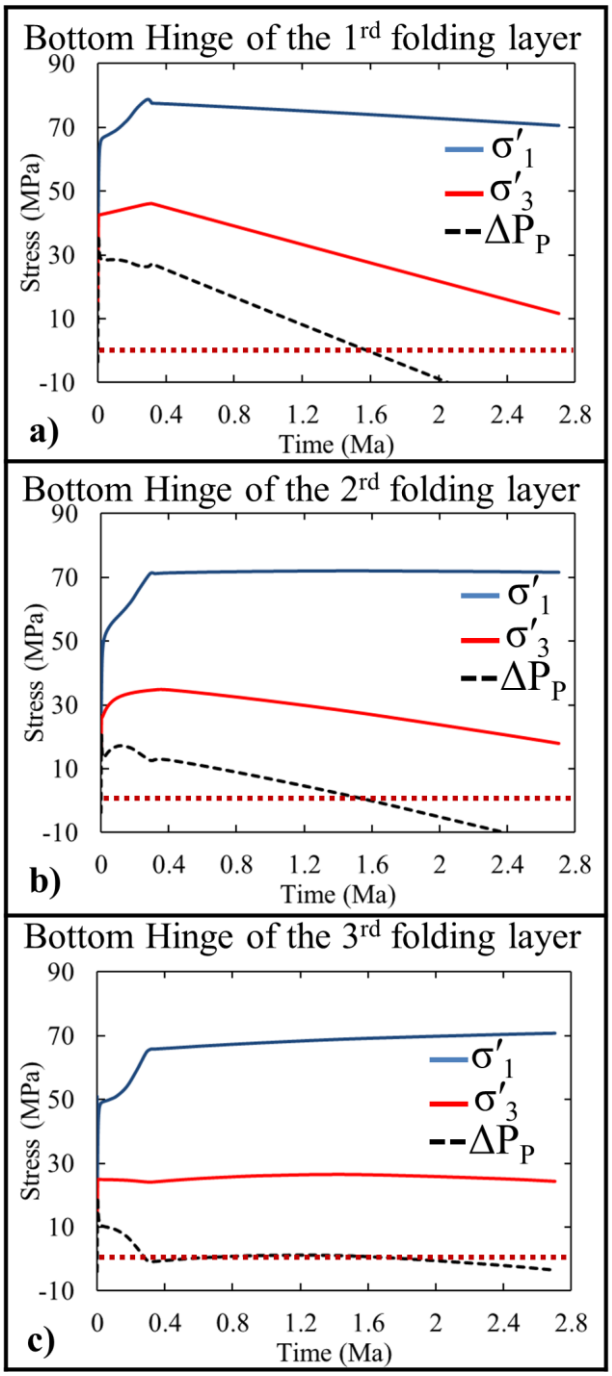

Figure 7: Effective principal stress evolution for Model 3 during erosional unloading.

3.4. MODEL 4

The stiffness and permeability distribution in Model 4 is equivalent to Model 2, although Model 4 features an initial overburden thickness of 3000 m and as a result of the increased compression ΔP_c magnitudes are much higher.

The top cap rock layer (Layer 2) displays ΔP_c magnitudes of ~41 MPa throughout the layer for 10% of shortening (Fig. 8a), 33-47 MPa for 20% of shortening (Fig. 8b), and 39-55 MPa for 30% of shortening (Fig. 8c). The second cap rock layer (Layer 4) shows slightly lower ΔP_c ranging from 25-31 MPa at 10% shortening, 27-33.5 MPa at 20%, and 23-31 MPa at 30%. The stress orientations throughout the shortening stages of the model are similar to Model 2.

In contrast to Model 3, the top cap rock layer (Layer 2) does not show imminent risk of fracture reactivation after 10% of shortening followed by erosional unloading over 2.06 Ma (with a remaining overburden thickness of 1071 m; Fig. 9a). ΔP_c magnitudes are ~13-17 MPa at the bottom of the hinge zone and ~7-10 MPa at the top of the hinge zone. The second cap rock layer has even higher ΔP_c magnitudes ranging from ~15 MP at the top of the hinge to 20-24 MPa at the bottom of the hinge. σ_1 is oriented horizontal in Layer 2 and at the top of the fold hinge in Layer 4.

For 20% followed by 2.3 Ma of erosion (with a remaining overburden thickness of 1292 m; Fig. 9b) ΔP_c magnitude contours are not layer sub-parallel anymore. For Layer 2, the lowest ΔP_c magnitudes are observed at the fold hinge zone with ΔP_c = 4-8 MPa at the bottom of the hinge and ΔP_c = 0 MPa at the top of the hinge. ΔP_c magnitudes in the fold limb increase towards ~17 MPa. For Layer 4, ΔP_c magnitudes are slightly higher ranging from ~13 MPa at the bottom of the hinge to ~9 MPa at the top of the hinge and increasing towards ~22 MPa in the fold limb.

The σ_1 orientations in Layer 2 are horizontal for the fold limb and the fold hinge zone; in the synform of the fold σ_1 becomes parallel to the hinge line. In Layer 4, σ_1 orientations are horizontal in the fold hinge and at an angle of ~45° to bedding in the fold limb.

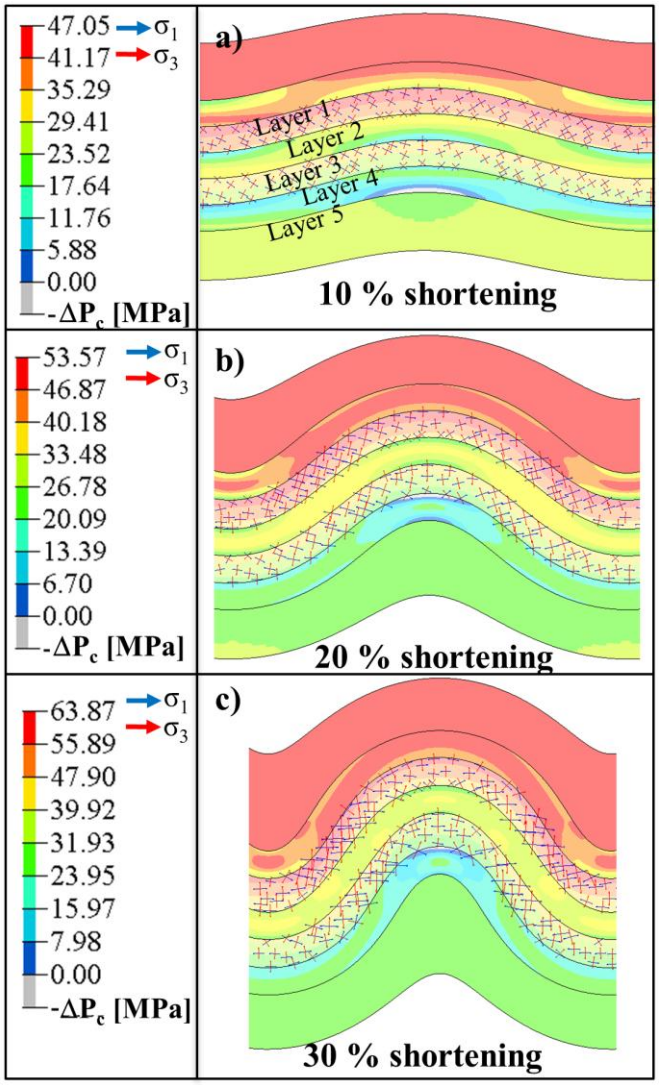

Figure 8: ΔP_c magnitudes for Model 4 for 10%, 20% and 30% of bulk shortening.

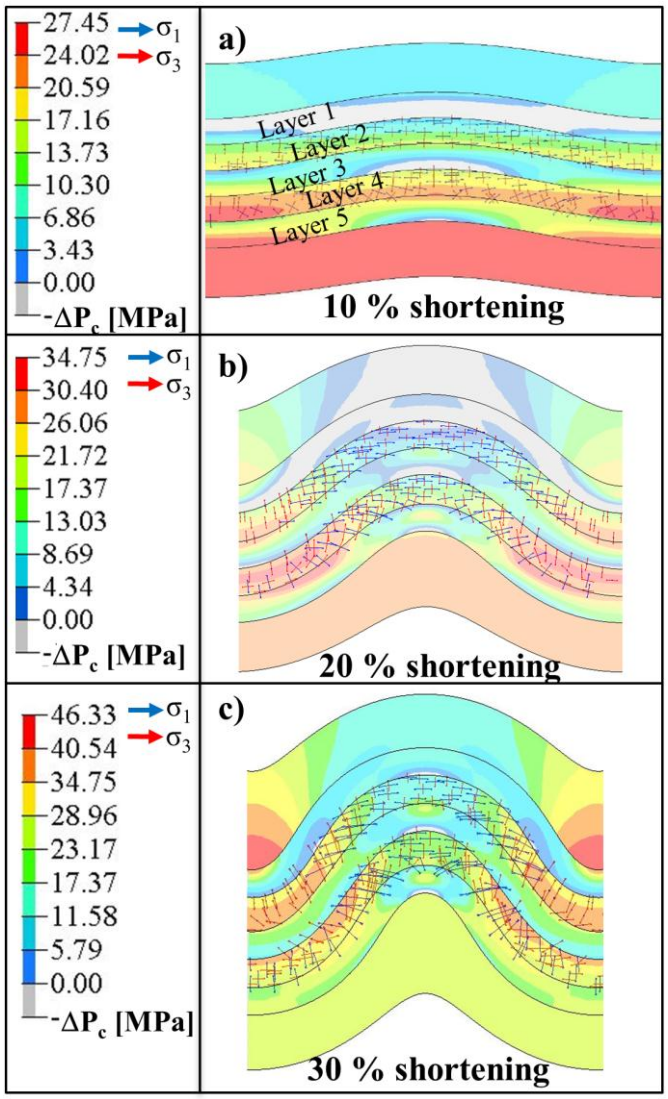

Figure 9: ΔP_c magnitudes for Model 4 after erosional unloading is applied.

For 30% followed by 2.039Ma of erosion (with a remaining overburden thickness of 2253 m; Fig. 9c) yields ΔP_c magnitudes in Layer 2 of 11-17 MPa in the hinge zone and 23-35 MPa in the fold limb. Layer 4 features ΔP_c magnitudes of 17-23 MPa in the hinge zone and 23-40 MPa in the limb. The stress orientations in both Layer 2 and 4 are similar to the 20% stage followed by erosion.

IV. Discussion

Recently, [20] have applied the PPSC concept to calculate ΔP_c of generic anticline structures under different stress regimes and considering different levels of inter-layer coupling using 3D finite element analysis. Their results show that ΔP_c results are strongly dependent on the relative location with respect to the injection location and are different for each combination of model parameters (such as stress regime and inter bedding friction coefficient). They conclude that in general the largest values of ΔP_c are obtained for a compressional stress regime and the lowest values of ΔP_c are obtained for an extensional stress regime, being in agreement with an earlier study by [10].

It should be recalled that the anticline models considered in [20] are based on static representations of stress and pore pressure, i.e. the specific strain path of how the geologic system evolved is not considered. As a result the ΔP_c magnitudes in [20] show much smaller variability. Based on

recent studies by [23-25], which show that principal stress and pore pressure magnitudes vary significantly throughout the deformation history of the fold and with respect to the permeability distribution of the modeled layers, the results of this study show and confirm that the evolution of ΔP_c also varies significantly.

4.1. COMPETENT CAP ROCK

For a scenario featuring stiff and more competent cap rock layers (Model 1), the early stages of deformation (10% of shortening) are characterized by a widespread risk of fracture reactivation (i.e. $\Delta P_c = 0$) at the bottom of the hinge zone throughout all cap rock layers (Layers 1, 3, 5; Fig. 3). As deformation progresses ΔP_c magnitudes in Layer 1 and 3 become significantly larger until at 30% shortening (ΔP_c = ~17.5 MPa in Layer 1; Fig. 3a), widespread failure is only observed for Layer 5 (Fig. 3b,c). In order to properly address the fracture reactivation risk the corresponding stress orientations of σ_1 and σ_3 have to be considered. For the regions characterized by ΔP_c =0 in the bottom of the cap rock hinge, σ_1 is horizontal and σ_3 is vertical at all deformation stages (Fig. 3). This corresponds to low angle thrust faults being optimally oriented for reactivation. For 30% of shortening at the top of the hinge in Layer 5, σ_1 is vertical and σ_3 is horizontal, making either high angle extensional faults or vertical extensional joints prone to reactivation. As stated by [35] fold hinge zones are characterized by low angle thrust faults at the bottom of the hinge and high angle extensional faults near the top of the hinge zone, hence making these regions an imminent risk of fracture reactivation.

The same layer configuration featuring a larger overburden thickness (Model 3) is characterized by much larger ΔP_c magnitudes due to the larger amount of compression and the risk of fracture reactivation is not imminent in any cap rock layer.

However, the results for Model 3 show that after the onset of erosional unloading, σ'_3 magnitudes drastically decrease, i.e. the differential stress increases, and hence ΔP_c magnitudes decrease rapidly, resulting in possible cap rock failure in Layers 1 and 3 for 10% and 20% of shortening followed by erosion. Erosional unloading has a larger effect (i.e. resulting in lower ΔP_c) for folds subjected to lower bulk shortening and the decrease in ΔP_c is largest for Layer 1 and lowest for Layer 5 (Fig. 6). This can be explained by the remnant strain stored in the respective fold layer [23]. Layer 5 features a narrower fold hinge and hence experiences more compression, which results in a slower decrease of ΔP_c (Fig. 7c).

The σ_1 orientations in the cap rock regions characterized by $\Delta P_c = 0$ at 10% followed by erosion are horizontal at the bottom of the hinge in Layer 1, corresponding to an imminent risk of fracture reactivation of low angle thrust fault likely to occur here [35]. The same fracture reactivation risk is evident at the bottom of the hinge zone in Layers 1 and 3 for the 20% and 30% stages followed by erosion. ΔP_c magnitudes of 0 are also observed in Layer 1 for 20% of shortening followed by erosion. The corresponding hinge line parallel σ_1 orientation and σ_3 being layer perpendicular would indicate reactivation of low angle thrust faults striking perpendicular to the hinge line. Such faults are not characteristic for buckle folds and have not been documented in the relevant literature [35]. More likely than the reactivation of these shear fractures is the onset/initiation of layer perpendicular tensile fractures when σ'_3 reaches 0 MPa for the case of prolonged erosion (Fig. 10). These tensile fractures are documented to occur frequently in buckle folds [35] and are likely to be initiated in buckle folds subjected to erosion [23].

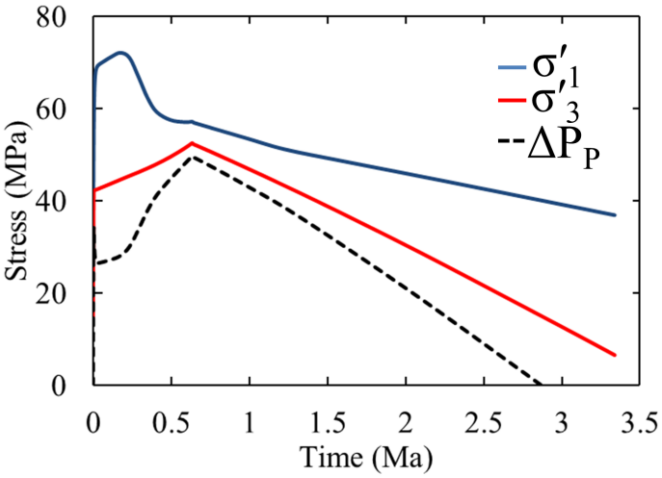

Figure 10: Effective principal stress evolution for Model 4 during erosional unloading in the limb of Layer 1.

4.2. INCOMPETENT CAP ROCK

In contrast to Model 1, Model 2 features cap rock layers that are less stiff and less competent. The results of Model 2 show that the cap rock layers are not at risk for fracture reactivation throughout the bulk shortening phase of deformation (Fig. 4). For all shortening stages the top cap rock layer (Layer 2) features the highest ΔP_c magnitudes. The stress orientations in Model 2 are not consistent with the orientations observed in Model 1 (which favor reactivation of frequently observed fracture sets) and thus provide an additional degree of safety as shear fractures oriented for reactivation due to the orientations in Model 2 (e.g. low angle thrust faults at the top of the hinge zone) are not likely to be observed in buckle folds [35].

It should also be noted that the possible injection layers (Layer 3 and 5) are characterized by fracture reactivation throughout the deformation history, which in turn has to be considered positive as the injectivity is increased in a fractured reservoir.

Similar to Model 3, the same layer configuration featuring a larger overburden thickness (Model 4) is characterized by much larger ΔP_c magnitudes (e.g. ΔP_c reaching up to 55MPa for 30%; Fig. 8c) due to the larger amount of compression and the risk of fracture reactivation is further reduced in both cap rock layers. Once erosional unloading is considered, ΔP_c

magnitudes are reduced but $\Delta P_c = 0$ is only obtained for 20% followed by erosion at the top of the hinge for Layer 2. The corresponding horizontal orientation of σ_1 would again favor low angle thrust faults at the top of the hinge, which are unlikely to occur here.

4.3. SUMMARY AND COMPARISONS

The results concerning the risk of fracture reactivation presented in this study show great variability in ΔP_c magnitudes depending both on the time in the deformation history of the fold as well as on the distribution of material properties. The combination of permeability distribution with the competence contrast in the respective cap rock – reservoir layer sequences is important. In general, low permeability in less competent layers (i.e. Model 2) results in greater ΔP_c magnitudes, with ΔP_c increasing for an increased amount of shortening. Risk of fault reactivation is not evident throughout the shortening process (i.e. $\Delta P_c > 0$) for all cap rock layers of the multi-layer fold system. For scenarios featuring low permeability in a competent layer (i.e. Model 1) cap rock failure is likely at the early stages of deformation for all cap rock layers, and only for later stages $\Delta P_c > 0$ in Layer 1 and 3; Layer 5 is always at risk of fracture reactivation. The differences between Model 1 and Model 2 can be explained by the lower differential stress resulting in the less competent layers, thus resulting in higher ΔP_c magnitudes. These results agree with [20] who also observe that if the cap rock is stiffer than the injection layer, ΔP_c may become 0 at the bottom of the hinge zone.

This study also shows that the process of erosional unloading needs to be considered for evaluating the risk of fracture reactivation of a geologic structure. Due to the decrease of σ'_3 the differential stress generally increases during erosion and as a result ΔP_c magnitudes decrease. This phenomenon again is more pronounced for scenarios featuring stiffer, more competent cap rock layers than injection/reservoir layers. E.g. once erosional unloading is considered for Model 4, ΔP_c magnitudes are reduced, but not as significantly as for Model 3. For example, ΔP_c magnitudes after 10% shortening followed by erosion are 7-17MPa in Layer 2 and 15-24 MPa in Layer 4. For the same stage of shortening + erosion, Model 3 shows ΔP_c magnitudes ranging from 0-7 MPa in Layer 1, 3.5-13 MPa in Layer 3, and 7-17 MPa in Layer 5. Furthermore, erosional unloading results in lower ΔP_c magnitudes in folded layers at the top of the multi-layer sequence. The lower layers are characterized by a higher degree of remnant compressional strain and thus the decrease in σ'_3 is less rapid [23].

In order to better visualize the effect of erosional unloading, 2 fold systems featuring less stiff cap rock layers are presented in Fig. 11. The multi-layer fold systems feature the same final overburden thickness (i.e. 1180 m), yet Model 5 (Fig. 11a) represents a fold that is under active shortening (20%), while Model 6 (Fig. 11b) represents a fold that had an initial overburden thickness of 3000 m and was subjected to erosional unloading. The difference in ΔP_c magnitudes is evident. Layer 2 in Model 5 has ΔP_c ranging from 11-17MPa (Fig. 11a); Layer 2 in Model 6 has ΔP_c ranging from 0MPa at the bottom of the hinge zone to 4-12 MPa at the top of the hinge and in the limb (Fig. 11b); Layer 4 in Model 5 has ΔP_c ranging from 4.5-11 MPa (Fig. 11a); Layer 4 in Model 6 has ΔP_c ranging from ~15 MPa at the bottom of the hinge to ~8MPa at the top of the hinge and 12-27 MPa in the limb (Fig. 11b). These differences while significantly affected by the decrease in σ'_3 as observed in Fig. 7, can be better understood by the evolution of the pore pressure in the fold system. The pore pressure distribution during the shortening stage (Fig. 11a) indicates hydrostatic values for the overburden and Layer 1, followed by over-pressure generated in the low permeability layers. As a result the pore pressure contours become layer parallel in the fold system. During the erosional unloading stage the over-pressure is significantly reduced, at a much higher rate as the hysdrostatic pore pressure in the overburden (Fig. 11b). The resulting under-pressure is in agreement with observations by [36,37] showing under-pressure evolution in 1D consolidation studies followed by elastic erosional unloading.

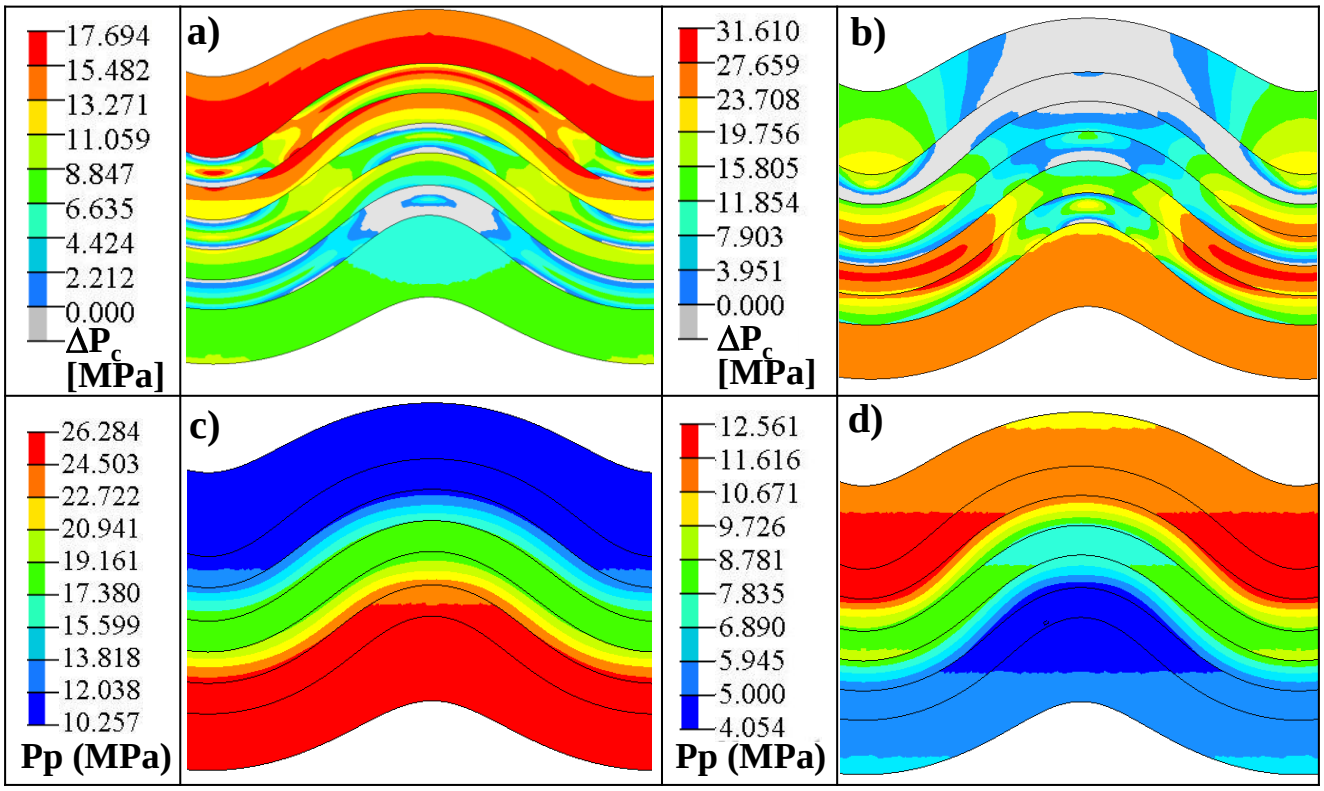

Figure 11: a) ΔP_c magnitudes for Model 5 featuring 20% of shortening with a remaining overburden of 1180 m. Grey contours represent zero critical pore pressure indicating failure. b) ΔP_c magnitudes for Model 6 featuring 20% of shortening with a remaining overburden of 1174 m after erosion. c) Pore pressure magnitudes for Model 5. d) Pore pressure magnitudes for Model 6.

IV. Conclusions

The concept of PPSC is extremely helpful as a first order risk assessment tool prior to subsurface fluid injection applications when the state of stress can be determined using numerical modeling approaches such as FEA. Based on the resulting 3D stress tensor, Eqs. (3 & 4) can be used to calculate the maximum sustainable pore pressure change, ΔP_c, in a formation before optimally oriented fractures are at risk of reactivation. The full 3D tensor based concept of PPSC is especially important for geologic structures which are characterized by a state of stress which is not Andersonian, i.e. where the vertical stress is not a principal stress (such as fold structures).

The results of this study show that the minimum ΔPc is varying throughout the deformation history of multilayer buckle folds and different locations within the structure show great variability in ΔP_c. Furthermore, the permeability distribution of the various layers in the multilayer fold system has great influence on minimum ΔP_c. If similar multi-layer buckle fold scenarios as presented in this study are considered for fluid injection applications the following points should be considered:

- Less competent (i.e. lower viscosity and Young's modulus) cap rocks should be preferred as larger ΔP_c magnitudes result.
- Injection in deeper settings (increased overburden thickness) provides larger ΔP_c magnitudes.
- If cap rocks represent stiff units, fold structures at a later stage of deformation should be preferred.
- Risk assessment of geologic structures needs to consider the deformation history of the structure, i.e. is erosional unloading present.
- Stress and pore pressure measurements are considered absolutely vital to calibrate site specific numerical models in order to benchmark the stress and strain history for realistic estimates of ΔP_c magnitudes.

It is clear that the numerical models presented are based on some limiting assumptions. As an outlook for future studies, the thermal evolution, especially during the erosional unloading process, needs to be considered as thermal contraction during exhumation will decelerate the evolution of under-pressure. The onset and initiation of fractures during the folding process can be added in the calculation of ΔP_c by including the rock cohesion into the equation system. Furthermore, fold structures in nature rarely resemble perfectly shaped cylindrical folds – the 3D state of stress in dome structures such as periclines will be different.

REFERENCES

[1] R.H. Sibson. "Brittle failure controls on maximum sustainable over-pressure in different tectonic stress regimes", *Bulletin American Society of Petroleum Geology*, v.87, p. 901-908, 2003.

[2] C.A. Barton, M.D. Zoback, and D.Moss. "Fluid flow along potentially active faults in crystalline rock", *Geology*, 23 (8), pp. 683-686, 1995.

[3] J.F. Gibbs, J.H. Healy, C.B. Raleigh, and J. Coakley. "Seismicity in the Rangely, Colorado, area: 1962–1970", *Bulletin Seismological Society of America*, 63, p. 1557–1570. 1973.

[4] R.L. Wesson, and C. Nicholson. "Earthquake Hazard Associated with Deep Well Injection", *Prepared by the U.S. Geological Survey*. Open-File Report 87-331, 1987.

[5] C. Frohlich, E. Potter, C. Hayward, and B. Stump. "Dallas-Fort Worth earthquakes coincident with activity associated with natural gas production", *The Leading Edge*, 29(3): p. 270-275, 2010.

[6] F. Cappa, and J. Rutqvist. "Impact of CO2 geological sequestration on the nucleation of earthquakes", *Geophysical Research Letters*, 38, L17313, 2011.

[7] J.P. Verdon, J.-M. Kendall, D.J. White, and D.A. Angus. "Linking microseismic event observations with geomechanical models to minimize the risks of storing CO2 in geological formations", *Earth Planet. Sci. Lett.*, 305, 1–2, p. 143–152, 2011.

[8] J.E. Streit, R.R. Hillis. "Estimating fault stability and sustainable fluid pressures for underground storage of CO2 in porous rock", Energy, 29, p. 1445-1456, 2004

[9] Q. Li, Z. Wu, Y. Bai, X. Yin, and X. Li. "Thermo-hydro-mechanical Modeling of CO2 Sequestration System Around Fault Environment", *Pure Appl. Geophys.*, 163, p. 2585-2593, 2006.

[10] J. Rutqvist, J. Birkholzer, F. Cappa, and C.-F. Tsang. "Estimating maximum sustainable injection pressure during geologic sequestration of CO2 using coupled fluid flow and geomechanical fault-slip analysis", *Energy Conversion and Management*, p. 1798-1807, 2007.

[11] J. Rutqvist, J. Birkholzer, F. Cappa, and C.-F. Tsang. "Coupled reservoir-geomechanical analysis of the potential for tensile and shear failure associated with CO2 injection in multilayered reservoir-caprock systems." *Int J Rock Mech Min Sci*, 45, p. 132-143, 2008.

[12] S. Vidal-Gilbert, J.-F. Nauroy, and E. Brosse. "3D geomechanical modeling for CO2 geologic storage in the Dogger carbonates of the Paris Basin", *Int. J. Greenhouse Gas Control*, V.3, Issue 3, p. 288-299, 2008.

[13] M.D. Zoback. "Managing the seismic risk posed by wastewater disposal", *Earth Magazine*, April 2, p. 38-43, 2012.

[14] A. Settari, and F.M. Mourits. "A Coupled Reservoir and Geomechanical Simulation System", SPE Journal, 3, p. 219–226, 1998.

[15] S.E. Minkoff, C.M. Stone, S. Bryant, M. Peszynska, and M.F. Wheeler. "Coupled fluid flow and geomechanical deformation modeling", *Journal of Petroleum Science and Engineering*, 38, p. 37–56, 2003.

[16] R. Dean, X. Gai, C. Stone, and S. Minkoff. "A Comparison of Techniques for Coupling Porous Flow and Geomechanics", SPE Journal, 11, p. 132–140, 2006.

[17] F. Cappa. "Influence of hydromechanical heterogeneities of fault zones on earthquake ruptures", *Geophys. J. Int.*, 185, p. 1049-1058, 2010.

[18] Q. Zhou, J.T. Birkholzer, C.-F. Tsang, and J. Rutqvist. "A method for quick assessment of CO2 storage capacity in closed and semi-closed saline formations", *International Journal of Greenhouse Gas Control*, 2, p. 626–639, 2008.

[19] A. Amirlatifi, A. Eckert, R. Nygaard, B. Bai, X. Liu, and M. Paradeis. "Role of Geometrical Influences of CO2 Sequestration in Anticlines", *46th US Rock Mechanics / Geomechanics American Rock Mechanics Assosiaction Symposium*. Chicago, IL, p. 12–255, 2012.

[20] A. Eckert, W. Zhang, X. Liu, and M. Paradeis, "Numerical estimates of the maximum sustainable pore pressure in anticline formations using the tensor based concept of pore pressure-stress coupling", *Journal of Rock Mechanics and Geotechnical Engineering*, V.7, 1, pp. 60-72, 2015.

[21] J.B. Altmann, T.M. Müller, B. Müller, M.R.P. Tingay, and O. Heidbach. "Poroelastic contribution to the reservoir stress path", *International Journal of Rock Mechanics and Mining Science*, 47, p. 1104–1113, 2010.

[22] J.B. Altmann, B. Müller, T.M. Müller, O. Heidbach, M.R.P Tingay, and A. Weißhardt. "Pore pressure stress coupling in 3D and consequences for reservoir stress states and fault reactivation", *Geothermics*, 52, p. 195-205, 2014.

[23] A. Eckert, P. Connolly, and X. Liu. "Large-scale mechanical buckle fold development and the initiation of tensile fractures", *Geochem. Geophys. Geosyst.*, 15, 11, p. 4570-4587, 2014.

[24] A. Eckert, X. Liu, and P. Connolly. "Pore Pressure Evolution and Fluid Flow during Visco-elastic Single-Layer Buckle Folding. *Geofluids*, in press, 2015.

[25] X. Liu, A. Eckert, and P. Connolly. "A Comparison of Stress Evolution in Single-layer and Multi-layer Buckle Folds. *The 49th US Rock Mechanics / Geomechanics Symposium*, San Francisco, CA, USA, 28 June- 1 July 2015.

[26] T. Engelder. "Loading paths to joint propagation during a tectonic cycle; an example from the Appalachian Plateau, USA", *Journal of Structural Geology*, 7, p. 459-476, 1985.

[27] T. Engelder, and M.P. Fischer. "Influence of poroelastic behavior on the magnitude of minimum horizontal stress, Sh, in overpressured parts of sedimentary basins", *Geology*, 22, p. 949–952, 1994.

[28] R.R. Hillis. "Coupled changes in pore pressure and stress in oil fields and sedimentary basins", *Petroleum Geoscience*, 7, p. 419–425, 2001.

[29] J.W.J. Rudnicki. "Fluid Mass Sources and Point Forces in Linear Elastic Diffusive Solids", *Mechanics of Materials*, 5, p. 383–393, 1986.

[30] J.C. Jaeger, N.G.W. Cook, and R.W. Zimmerman. "*Fundamentals of Rock Mechanics*", 4th Edition. ed. John Wiley & Sons, 2007.

[31] S.M. Schmalholz, and Y.Y. Podladchikov. "Buckling versus folding: importance of viscoelasticity", *Geophysical Research Letters*, 26(17), p. 2641-2644, 1999.

[32] S.M. Schmalholz, Y.Y. Podladchikov, and D.W. Schmid. "A spectral/finite difference method for simulating large deformations of heterogeneous, viscoelastic materials", *Geophysical Journal International*, 145(1), p.199-208, 2001.

[33] C.R. Medina, J.A. Rupp, and D.A. Barnes. "Effects of reduction in porosity and permeability with depth on storage capacity and injectivity in deep saline aquifers: A case study from the Mount Simon Sandstone aquifer", *International Journal of Greenhouse Gas Control*, 5(1), p.146-156, 2011.

[34] R.J. Twiss, And E.M. Moores. "Structural Geology", 2nd Edition, W.H. Freeman and Company, New York, 2007.

[35] N.J. Price, and J.W. Cosgrove. "Analysis of Geological Structures". Cambridge University Press, UK 1990.

[36] J.J. Jiao., and C. Zheng. "Abnormal fluid pressures caused by deposition and erosion of sedimentary basins", *J. Hydrol.*, 204(1), p.124-137, 1998.

[37] S. Ellis, and D. Darby. "A modified Terzaghi consolidation factor for first-order estimation of overpressure resulting from sedimentation: review and synthesis", Math. Geol., 37(1), p.115-123, 2005.